Journal of Materials Chemistry A

ROYAL SOCIETY OF CHEMISTRY

PAPER

View Article Online
View Journal | View Issue

Cite this: J. Mater. Chem. A, 2024, 12, 17422

Understanding the impact of Bi stoichiometry towards optimised $BiFeO_3$ photocathodes: structure, morphology, defects and ferroelectricity†

Haozhen Yuan, Subhajit Pal, Chloe Forrester, Qinrong He and Joe Briscoe *

$BiFeO_3$ thin films have been widely studied for photoelectrochemical water splitting applications because of its narrow bandgap and good ferroelectricity which can promote the separation of photo-generated charges. Bismuth is well known as a volatile element and excess bismuth is usually added into the precursor to compensate the loss of bismuth during heat treatment, but the amount of excess bismuth required and how excess bismuth will affect PEC performance have not been clearly studied. Herein, self-doped $Bi_{1+x}FeO_3$ thin films are prepared *via* simple chemical solution deposition method with excess bismuth from 0–30% in the precursor. The loss of bismuth after annealing is confirmed by EDX and XPS. Multiple factors were investigated and it was found that non-stoichiometric Bi resulted in changes of structure, morphology, defects, electronic properties and PEC performance. An enhanced photocurrent is observed in bismuth-rich $BiFeO_3$ films, which can be ascribed to the larger grain size, decreased oxygen vacancies, lattice distortion and supported charge separation. Moreover, the photocathodic performance can be further enhance by ferroelectric poling. Our work indicates that deficient bismuth should be carefully avoided during heat treatment and moreover, a slight excess of Bi is beneficial for PEC performance. Therefore, we offer a simple way to enhance PEC performance of $BiFeO_3$-based ferroelectric materials through careful control of their stoichiometry.

Received 15th September 2023
Accepted 6th June 2024

DOI: 10.1039/d3ta05617a

rsc.li/materials-a

1. Introduction

Rapidly growing energy demand leads to research on the development of sustainable energy resources. Therefore, the production of environmentally friendly hydrogen from renewable energy resources is a promising strategy. In this regard, photocatalytic (PC) or photoelectrochemical (PEC) processes are considered a potential route for producing sustainable hydrogen directly from solar illumination. Many studies have been performed for photochemical water splitting utilising conventional semiconductors as photoelectrodes. However, the high recombination rate of photo-generated charges of conventional semiconductors hinders the development of PEC application. In this context, ferroelectric materials having spontaneous polarisation response have attracted much attention.[1] The domains inside ferroelectrics can be reversibly switched by external bias and an internal electric field can remain due to the remnant polarisation after removing the external electric field, which favours the separation of photo-generated holes and electrons.[2,3] For this reason, employment of ferroelectric materials has been considered as an effective approach to improve photocatalytic activity.[4]

However, typical ferroelectric materials, such as $PbTiO_3$,[5,6] $BaTiO_3$ (ref. 7–9) and $Pb(Zr, Ti)O_3$,[10] have wide bandgap normally larger than 3.2 eV, which are only active in the ultraviolet range, hence, reduces the PEC performance. Therefore, $BiFeO_3$, which possesses a bandgap around 2.2–2.7 eV along with significant polarisation response (P_r ranges from 60–150 μC cm^{-2})[11–17] has been considered as a promising candidate as photoelectrode for water splitting. The effects of BFO film thickness on PEC performance were reported by Liu *et al.*,[18] where 200 nm BFO photocathodic film showed the highest photocurrent density of 15 μA cm^{-2}. Moreover, BFO with remnant polarization oriented into the film ('downward' polarization) exhibited better PEC performance due to the band bending associated with the screening of the polarization at the interface. Also, Wang *et al.* found that O_2-annealed BFO acted as photoanode and exhibited the photocurrent density of 70 μA cm^{-2} at 1.23 V_{NHE}.[19]

The commonly used methods to prepare $BiFeO_3$ nanoparticles or films are solid-state synthesis[20,21] and chemical solution deposition (CSD). Both need an annealing process with a high temperature above 500 °C. Importantly, it is known that

School of Engineering and Materials Science, Queen Mary University of London, London, E1 4NS, UK. E-mail: j.briscoe@qmul.ac.uk

† Electronic supplementary information (ESI) available. See DOI: https://doi.org/10.1039/d3ta05617a

Bi is volatile and easily evaporated at high temperature, which leads to nonstoichiometric $BiFeO_3$.[22] Therefore, excess Bi is usually added to compensate for the Bi loss during annealing. The effects of excess Bi on the structure and ferroelectricity of $BiFeO_3$ has been studied extensively. Tian *et al.* prepared non-stoichiometric BFO films through a laser molecular beam epitaxy system (Laser-MBE).[23] The BFO targets had different Bi/Fe ratio from 0.8–1.5. It was found that Bi-excess films exhibit upward uniform polarisation while Bi-deficient films show downward uniform polarisation. Additionally, Kumari *et al.* reported that the remnant polarisation of BFO nanoparticle with 5% excess Bi was 77% higher than that of stochiometric BFO nanoparticles while an increased bandgap was observed in BFO with excess Bi.[24] Gupta *et al.* also found that BFO thin films with 5% excess Bi have higher remnant polarization[25] compared to stoichiometric ones, while Xie *et al.*[22] studied BFO with different excess Bi content (from 0–15%) and showed that BFO with 10% excess Bi exhibited the highest remnant polarisation and lowest leakage current density. Therefore, the different Bi-content in BFO samples has been shown to significantly vary its structural, ferroelectric, and optical properties. However, the effect of different Bi-content on the performance in photoelectrochemical applications is lacking in the literature.

Additionally, various properties of ferroelectric films can affect photoelectrochemical performance, including material structure, morphology, optical properties, oxygen vacancies and ferroelectricity. To date, the strategy of A-site doping, B-site doping and A & B-site co-doping has been employed for enhanced ferroelectric properties in BFO. Rare-earth elements such as La,[26–28] Sm,[29] Gd,[30,31] Nd,[32] and Er[33] have been widely studied for A-site substitution, while transition elements, such as Mn,[34,35] Co[36] and Ti,[28] have been employed for B-site substitution to modify the structure and ferroelectric properties of BFO, hence influence the PEC performance. A transition from ferroelectric rhombohedral structure (*R3c*) to paraelectric orthorhombic structure (*Pnma*) is sometimes found in many BFO doping studies.[28,35] Also, a change of morphology is usually observed along with modification. For example, Reddy *et al.* have demonstrated that the grain size decreased from 194 nm to 73 nm when La-dopant addition was varied from 0 to 10%.[26] Consequently, the photocatalytic, magnetic, and electrochemical properties were found to be improved in the BFO nanoparticles. Moreover, it is also noticed that oxygen vacancies have been considered as an important factor in PEC performance.[37]

Thus, in this work, we carry out an in-depth investigation to understand the relationship between Bi-content and photoelectrochemical performance by studying the correlation with the structural, ferroelectric and optical properties. We prepare $Bi_{1+x}FeO_3$ thin films as photocathodes by a simple chemical solution deposition method which allows large-scale coating capability. It is found that the PEC performance can be enhanced by controllable amounts of excess bismuth in the precursor solution. In addition, the PEC performance can be further enhanced *via* an electrochemical poling treatment to enhance the ferroelectric properties. This paves the way to develop $BiFeO_3$-based ferroelectric materials with careful stoichiometric control for PEC applications.

2. Experimental details

2.1 Film preparation

$Bi_{1+x}FeO_3$ ($x = 0$, 5, 10, 15, 20, 25 and 30%) thin films, named as BFO_0, BFO_5, BFO_10, BFO_15, BFO_20, BFO_25 and BFO_30 subsequently, were prepared by a simple chemical solution deposition method.[19] All chemicals were purchased from Sigma-Aldrich unless otherwise specified.

$Bi_{1+x}FeO_3$ films were deposited on 20 × 25 mm^2 fluorine-doped tin oxide (FTO) glass substrates (Sigma-Aldrich, 2.2 mm thickness, surface resistivity ~7 Ω sq^{-1}), which were sonicated sequentially in deionized water, acetone and 2-propanol for 10 minute each for cleaning. The precursor was prepared as the following steps. Bismuth(III) nitrate pentahydrate ($Bi(NO_3)_3 \cdot 5H_2O$, 98%) was firstly dissolved in mixed solvent with 2-methoxyethanol (anhydrous, 99.8%) and acetic acid (glacial, ≥99.7%) and then iron(III) nitrate nonahydrate ($Fe(NO_3)_3 \cdot 9H_2O$, 98%) was added. The volume ratio of 2-methoxyethanol to acetic acid was 3 : 1 and the concentration of the iron source was fixed at 0.5 M while that of bismuth source was adjusted with different x. The precursor solution was stirred for around 20 hours and then spin-coated at 3000 rpm for 30 seconds, followed by heating at 90 °C for 1 minute and 350 °C for 5 minutes in air. Finally, as-prepared films were annealed at 650 °C for 1 hour in a tube furnace in air and then cooled down to room temperature at a ramp rate of 5 °C min^{-1}.

2.2 Characterization methods

The crystalline structure of $Bi_{1+x}FeO_3$ thin films was investigated by X-ray diffraction (XRD) using a PANalytical X'Pert Pro diffractometer, equipped with a Cu Kα source, with a 0.5° grazing incidence angle. The XRD measurements were obtained from 2θ = 20 to 70° with a scan speed of 0.006° s^{-1}. The morphology of the samples was studied using a scanning electron microscopy (FEI Inspect F), using an accelerating voltage of 5 kV. The analysis of size distribution was performed using Nanomeasurer software. More than 300 grains were measured to calculate the grain size distribution in each image (Fig. S1†). A PerkinElmer Lambda 950 UV-Vis spectrophotometer was employed for the measurement of absorption in range of 300–700 nm. The optical bandgap of $Bi_{1+x}FeO_3$ was estimated using the Tauc plot method. For better understanding of the non-stoichiometric systems, the chemical states of atoms and their atomic concentration on the surface were investigated by X-ray photoelectron spectroscopy (XPS). All peaks in XPS spectra were calibrated to the adventitious C 1s peak at 284.8 eV. The surface Bi/Fe atomic ratio was calculated from the narrowed scan of Fe 2p (Fig. S2†) and Bi 4f (Fig. S3†) XPS spectra using eqn (1) (ref. 38) where c(Bi) and c(Fe) represent atomic concentration of elemental Bi and Fe in BFO films; $A_{Bi_{4f}}$ and $A_{Fe_{2p}}$ represent the area of Bi4f and Fe2p peaks respectively; $S_{Bi_{4f}}$ and $S_{Fe_{2p}}$ represent the sensitivity factor of Bi4f and Fe2p; $S_{Bi_{4f}} = 38.304$ and $S_{Fe_{2p}} = 14.353$.

$$\frac{c(\mathrm{Bi})}{c(\mathrm{Fe})} = \frac{A_{\mathrm{Bi_{4f}}}/S_{\mathrm{Bi_{4f}}}}{A_{\mathrm{Fe_{2p}}}/S_{\mathrm{Fe_{2p}}}} \quad (1)$$

Ultraviolet photoelectron spectroscopy (UPS) was employed to determine the work function and Fermi level position of $Bi_{1+x}FeO_3$. This was then combined with the XPS valence band measurements and UV-Vis to obtain the band diagram consisting of the position of conduction band, valence band and Fermi level.

2.3 Photoelectrochemical measurements

A three-electrode configuration was used for photoelectrochemical measurements.[39] Ag/AgCl, a platinum wire and $Bi_{1+x}FeO_3$ thin film were employed as reference electrode, counter electrode and working electrode respectively. Linear sweep voltammetry (LSV) measurements were carried out using a potentiostat (Gamry Potentiostat Interface 1000) in 0.2 M Na_2SO_4 electrolyte, which was scanned from −0.7 V–1.0 V *vs.* Ag/AgCl at a rate of 10 mV s^{-1}. Illumination was from a Xe-lamp solar simulator, which was calibrated to AM 1.5 G 1 sun (100 mW cm^{-2}). The applied potential *vs.* Ag/AgCl reference electrode was converted to the reversible hydrogen electrode (RHE) using the eqn (2):

$$E_{\mathrm{RHE}} = E_{\mathrm{Ag/AgCl}} + E^{\circ}_{\mathrm{Ag/AgCl}} + 0.059\mathrm{pH} \quad (2)$$

where $E^{\circ}_{\mathrm{Ag/AgCl}} = 0.197$ V at 25 °C and pH of 0.2 M Na_2SO_4 is 6.5. The PFM measurements were carried out using a Bruker ScanAsyst Dimension AFM (Nanoscope-6) system in contact resonance mode. All the PFM measurements were performed using platinum and iridium-coated tips (SCM-PIT-V2, Bruker) with a force constant of 3 N m^{-1}. PFM measurements were performed in the capacitor geometry by applying the bias voltage to the probe and the bottom electrode was grounded. To investigate the ferroelectric properties, a DC voltage of ±8 V was applied, after which the PFM phase images were collected. KPFM measurements were carried out in peak-force KPFM mode for the contact potential difference between BFO films and the probe which is the same as that used in PFM measurements. In order to measure surface photovoltage, a 391 nm LED light source was employed during KPFM measurements under illumination. To investigate the effects of ferroelectric polarization on photoelectrochemical performance, electrochemical poling (EC poling) was conducted using a Keithley 2400 by applying alternatively ±8 V on a platinum counter electrode for 5 steps.[40] For negative poling, it followed the 5 steps as −8, +8, −8, +8 and −8 V and each step lasted for 10 seconds, while for positive poling, it started and finished at +8 V.

3. Results and discussion

It can be observed from SEM images that all $Bi_{1+x}FeO_3$ thin films show compact morphology with a small number of pinholes at the interval of grains (Fig. 1). Additionally, the grain size increases with increasing Bi content up to BFO_15 followed by a decreasing trend observed with further increasing x, which indicates that the excess bismuth has a major effect on film morphology. The grain size distribution histogram of each film can be found in Fig. S1.† Moreover, the size distribution in Fig. S1† indicates that larger grains become more prevalent in BFO_15, which maximizes the mean size while the dominance of small grains leads to reduction of mean size when further excess bismuth is added (Fig. 1h). The trend of change in size is the same as Xie's study.[22] The mean thickness of BFO_10 is 170 (+27.4, −26.7) nm according to the cross-sectional SEM images in Fig. S4.† The loss of bismuth may result in the appearance of bismuth vacancies or the occupation of the empty Bi sites by smaller iron cations, which leads to crystal shrinkage. Thus, the early increase can be attributed to the compensation of bismuth volatilization while the later reduction may be explained by the occurrence of secondary phases Bi_2O_3 or $Bi_{25}FeO_{40}$ at grain boundaries, which suppresses the growth of BFO. This is supported by EDX, XPS and XRD data discussed below, which shows that BFO_10 and BFO_15 are the closest to stoichiometry, and secondary phases begin to appear from BFO_20 and are very large in BFO_30.

EDX results in Fig. 2a confirm the bismuth loss during preparation, which is ascribed to the volatility of bismuth oxide under heat treatment. Thus, almost all studies on BFO films utilize excess bismuth source for compensation. XPS and EDX give similar Bi/Fe atomic ratio results up to BFO_20 as shown in Fig. 2a. The films are Bi deficient with less than 10% excess bismuth added because of bismuth loss during heat treatment, while with more than 10% excess bismuth added the films are Bi-rich. In BFO_10, it is nearly stoichiometric, taking both XPS and EDX data into account. In BFO_25 and BFO_30 the XPS and EDX data begin to deviate with much higher Bi content measured by XPS. This correlates with the appearance of the Bi_2O_3 secondary phase in XRD measurements discussed below, which suggests that this secondary Bi_2O_3 phase forms on the surface, since XPS only collects a signal from the top ~5 nm of the sample, whereas EDX signal will be collected from the whole film at this film thickness.

In principle, the introduced defects could have an effect on the chemical states of iron or oxygen. The excess A-site cation (Bi) should cause B-site iron vacancies with net negative charges in the lattice and, therefore, result in increased oxygen vacancies or cation valent states because of charge compensation to maintain electrical neutrality.[41,42] As shown in Fig. S2,† narrowed scan of $Fe2p_{3/2}$ XPS spectra can be fitted by 3 peaks, Fe^{2+} $2p_{3/2}$, Fe^{3+} $2p_{3/2}$ and Fe^{4+} $2p_{3/2}$. The coexistence of Fe^{2+}, Fe^{3+}, and Fe^{4+} are found in all $BiFeO_3$ films. However, the concentration of Fe^{2+}, Fe^{3+}, and Fe^{4+} remains the same indicating the changing Bi stoichiometry does not affect Fe site occupancy.

Fig. 2b shows XPS patterns of the O1s peaks in $BiFeO_3$ films. The peaks around 529.3 (±0.1 eV) and 531 (±0.2 eV) correspond to lattice oxygen O_L and oxygen vacancy environment O_V respectively.[37] The concentration of oxygen vacancies can be analysed by the RIR (relative intensity ratio) of O_V/O_L, where lower RIR values correspond to less oxygen vacancies in the BFO films. The oxygen vacancies gradually decrease from 30.0 (±0.1)% in BFO_0 to 22.7 (+0.4, −0.2)% in BFO_20 and remains

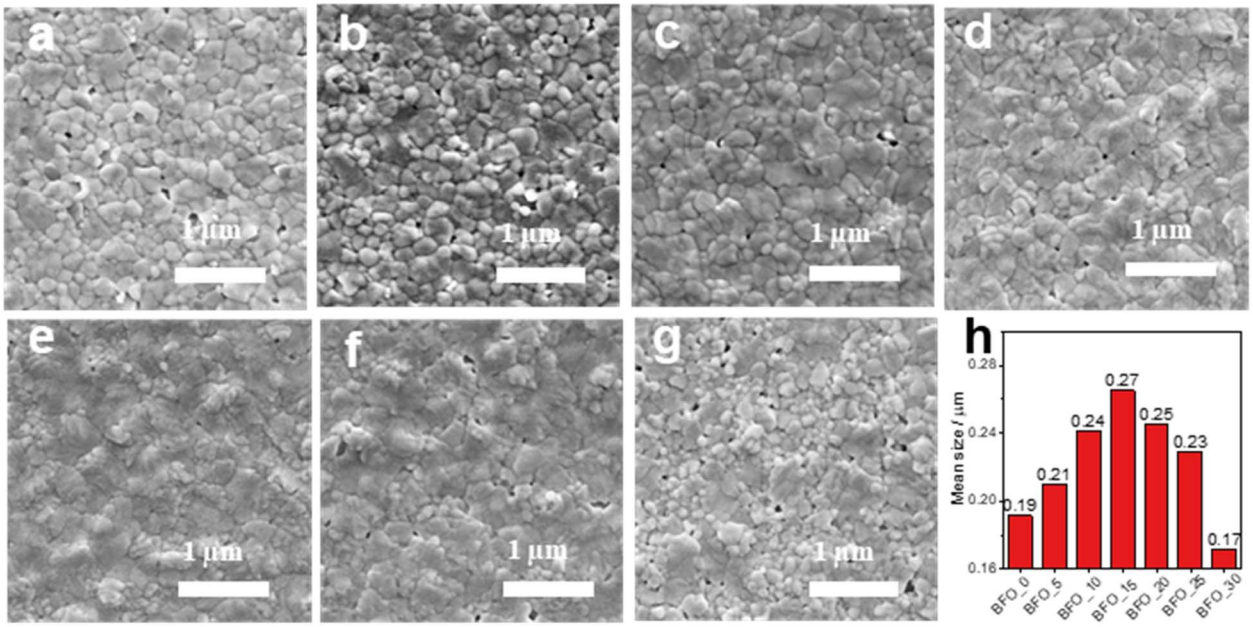

Fig. 1 Top-view SEM images of BFO_0 (a), BFO_5 (b), BFO_10 (c), BFO_15 (d), BFO_20 (e), BFO_25 (f) and BFO_30 (g) and bar chart of mean size (h). The size distribution was fitted using a lognormal function (Fig. S1†). The mean grain sizes are 0.19, 0.21, 0.24, 0.26, 0.24, 0.23 and 0.17 μm respectively.

approximately constant within error for BFO_25 and BFO_30. As discussed above, there is no difference in the chemical states of iron, therefore, the decrease in oxygen vacancies should be ascribed to the compensation of bismuth loss in Bi-deficient BFO_0 to BFO_10. The more bismuth added, the less bismuth deficient and the less oxygen vacancies generated. For BFO with

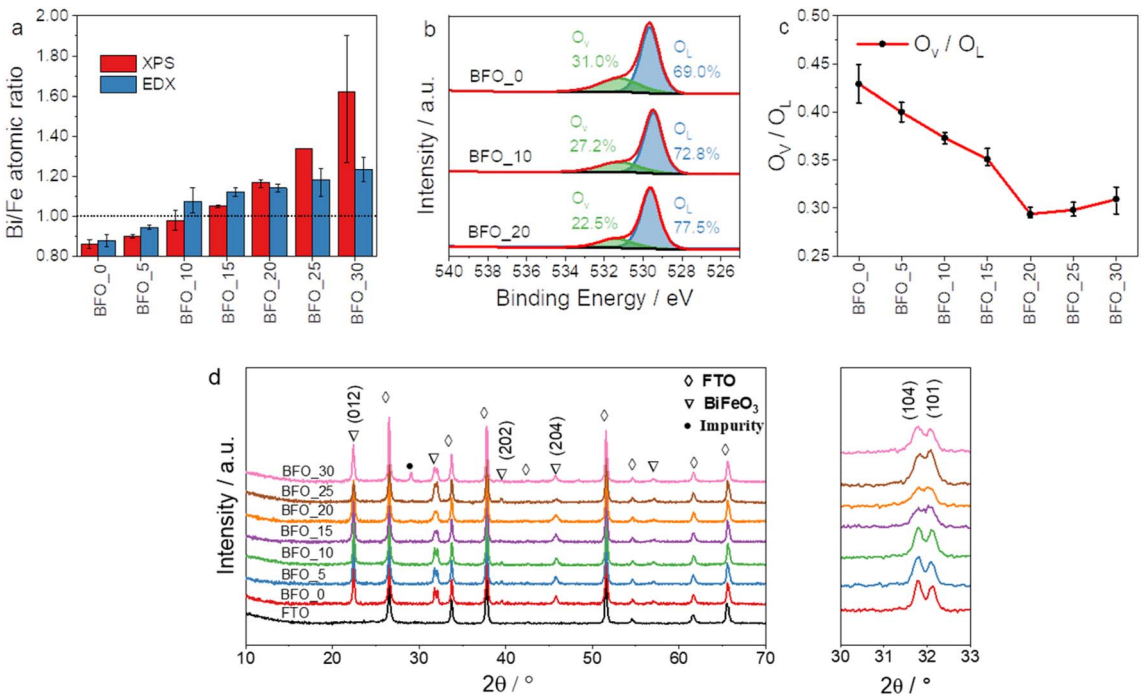

Fig. 2 (a) Measured Bi/Fe atomic ratio *via* XPS (0.86, 0.9, 0.98, 1.05, 1.17, 1.34 and 1.62 for BFO_0 to BFO_30 respectively) and EDX (0.88, 0.95, 1.07, 1.12, 1.14, 1.18 and 1.23 for BFO_0 to BFO_30 respectively); (b) XPS O_{1s} scan of BFO_0, BFO_10 and BFO_20 fitted with O_L (lattice oxygen) and O_V (oxygen vacancy) peaks; (c) the relative intensity ratio of O_V/O_L of $Bi_{1+x}FeO_3$ films and (d) X-ray diffraction patterns of $Bi_{1+x}FeO_3$ thin films with enlarged pattern around $2\theta = 32°$.

more than 15% excess bismuth added in the precursor, it becomes a bismuth-excess system. The further reduction in oxygen vacancies can be explained by the interstitial bismuth or substitution of the B-site in lattice, in which situation oxygen vacancies decrease to retain charge neutrality.

X-ray diffraction (XRD) analysis was performed on $Bi_{1+x}FeO_3$ thin films as shown in Fig. 2d to investigate the crystal structure and presence of secondary phases as a function of Bi-content. According to XRD patterns of BFO_0 to BFO_10, distinct peaks at 22.4°, 31.8°, 32.1°, 38.9°, 39.6°, 45.7°, 56.4° and 57.0° can be indexed to $BiFeO_3$ (012), (104), (110), (006), (202), (204), (018) and (300) planes, respectively, which matches the rhombohedral (*R*3*c*) structure (ICSD-29921) well. There is no $Bi_2Fe_4O_9$ and $Bi_{25}FeO_{40}$ which usually grow as secondary phases. It indicates that the slight fluctuation around stoichiometry does not have a major effect on the structure, which remains rhombohedral. Whereas, with further excess bismuth introduced in BFO_15 and BFO_20, the doublet peaks (104) and (101) around 32° tends to merge into one single peak, which indicates distortion in the lattice. The merging of doublet peaks around 32° is usually observed in doped BFO, such as A-site substitution with Ca,[43] La,[44] which are explained by the structure distortion due to the different ionic radii of foreign dopants. Similarly here, such transition and absence of secondary phases prove that excess bismuth enters the lattice structure. With further excess bismuth (BFO_25), the doublet peaks recover, and the splitting becomes clear in BFO_30. Meanwhile, an impurity peak at 29° which might be attributed to Bi_2O_3 appears and grows in intensity in BFO_30. The competition between the formation of impurities and defects inside BFO lattice can therefore explain this phenomenon. When there is enough excess bismuth, it will preferentially form Bi_2O_3. As the excess Bi has then been accommodated within the Bi_2O_3 secondary phase, the main $BiFeO_3$ phase is able to relax to the original rhombohedral structure.

The absorption spectra of $Bi_{1+x}FeO_3$ thin films were measured to investigate their optical properties. In Fig. 3a, they show band edges within 400–460 nm. All spectra share a similar shape of plot and the difference of absorption among all samples is negligible and does not show any overall trend. Tauc plots were employed for analysis of bandgap using the following formula:[45]

$$(\alpha h\nu)^{1/r} \propto (h\nu - E_g) \quad (3)$$

where, α is absorption coefficient, h is the Planck's constant, ν is the frequency of light, E_g is the band gap energy and the exponent $1/r$ denotes the nature of the transition, $r = 1/2$ for direct allowed transitions and $r = 2$ for indirect allowed transitions.[46] The bandgap was estimated using the Tauc plots presented in Fig. 3b. The direct bandgap of $Bi_{1+x}FeO_3$ thin films are all 2.72 ± 0.2 eV, corresponding to the value in the literature.[47,48] The result indicates that the excess bismuth has no effects on the optical property of $BiFeO_3$ thin films.

After confirming the structure, morphology, optical properties and chemical states, we tested their photoelectrochemical properties under chopped illumination in 0.2 M Na_2SO_4 electrolyte. In Fig. S5 and S6,† negative photocurrent was found for all $Bi_{1+x}FeO_3$ thin films, which is consistent with photocathodic properties. As shown in Fig. 4a and b, bismuth-rich film BFO_20 shows a much higher photo-generated current density than stoichiometric BFO_10 while the bismuth-deficient film BFO_0 exhibits the lower photocurrent density. Especially, the photocurrent density of BFO_20 (45.58 μA cm^{-2}@0.2 V *vs.* RHE) is enhanced by 66.6% when compared with the stoichiometric film BFO_10 (27.35 μA cm^{-2}@0.2 V *vs.* RHE). The enhanced photocurrent in BFO_20 was also confirmed by C-AFM photocurrent images in Fig. S7† where much brighter regions occur in BFO_20 indicating a higher photocurrent. In general, the photocurrent follows an increasing trend with more bismuth present in the films until BFO_20. With further bismuth added, the photocathodic current drops to 22.96 μA cm^{-2} (@0.2 V *vs.* RHE) in BFO_30 film (Fig. 4c). The onset potential (shown in Fig. S5†) also shares a similar trend as photocurrent values. It increases from 0.03 $V_{Ag/AgCl}$ (BFO_0) to 0.15 $V_{Ag/AgCl}$ (BFO_20) and decreases again for BFO_25 and further for BFO_30. The LSV curves measured with reverse scanning direction from −0.6 to 0.6 V *vs.* Ag/AgCl in Fig. S10† show the same trend and close match of the photocurrent density as those in Fig. 4a and b.

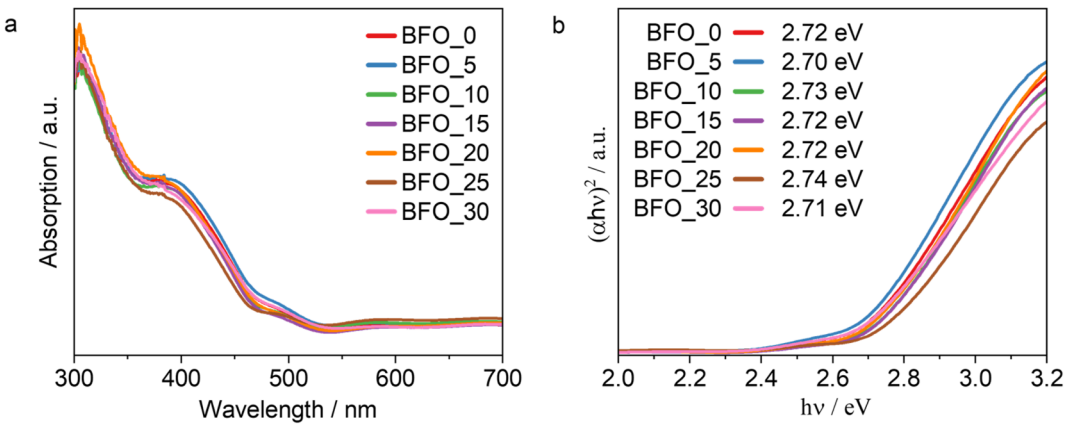

Fig. 3 (a) Absorption spectra and (b) Tauc plot of $Bi_{1+x}FeO_3$ films.

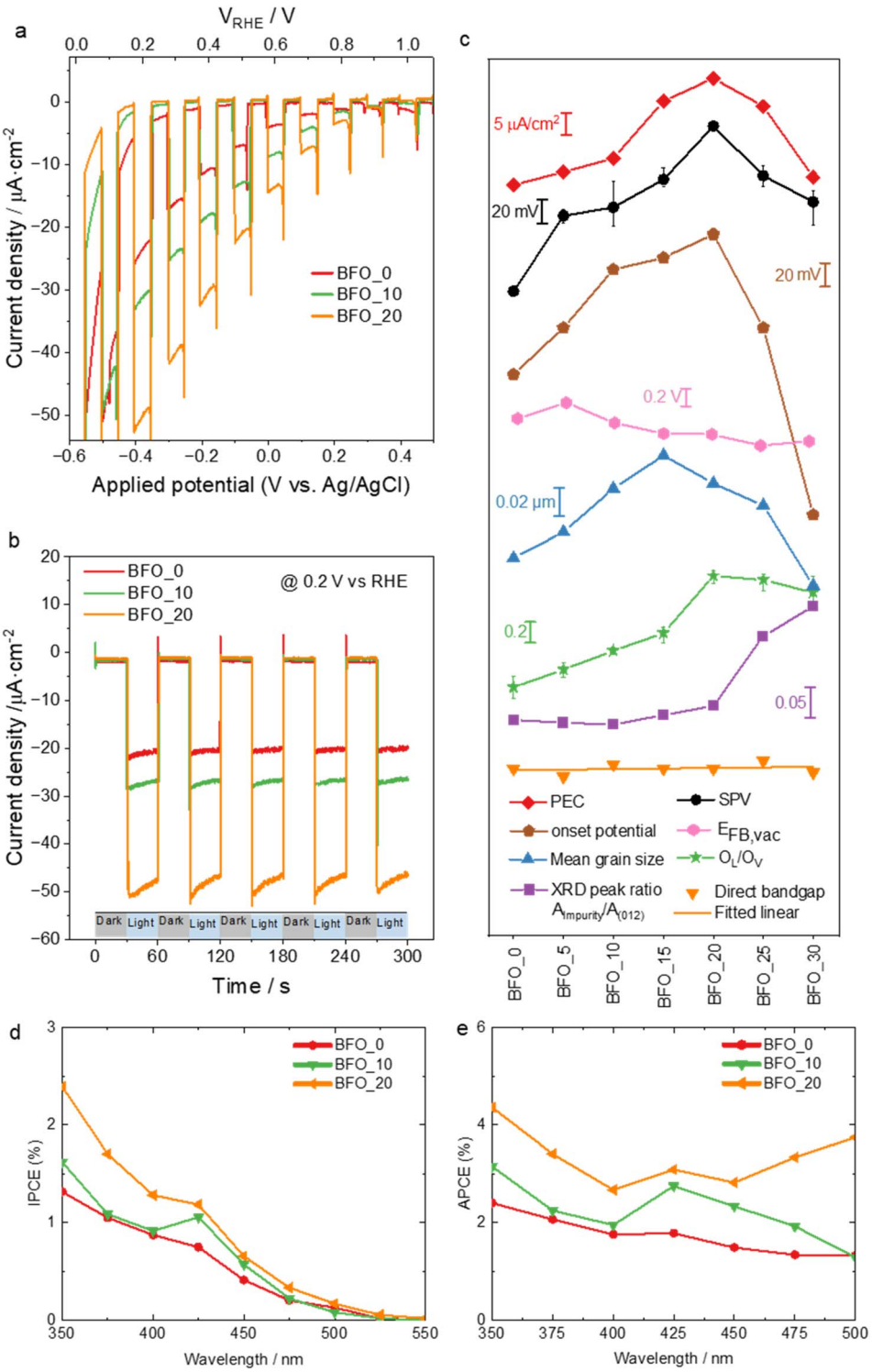

Fig. 4 (a) LSV measurements of BFO_0, BFO_10 and BFO_20 thin films under chopped illumination in 0.2 M Na_2SO_4 electrolyte with the scanning direction from 0.6 to −0.6 V *vs.* Ag/AgCl; (b) stability test measured at 0.2 V *vs.* RHE for 300 s with dark and light chopped condition; (c) the correlation among photocurrents and other factors including SPV, grain size, oxygen vacancies, impurity phase, estimated flat band potentials in vacuum and bandgap. All lines except for bandgap trend are guides to eye; (d) IPCE and (e) calculated APCE spectrum of 3 thin films, BFO_0, BFO_10 and BFO_20.

The incident photon–current conversion efficiency (IPCE) in Fig. 4d further confirmed the enhanced PEC performance of Bi-excess BFO films (BFO_20) and also closely matches the UV-Vis absorption spectra shown in Fig. 3a. In Fig. 4e, the absorbed photon-to-current conversion efficiency (APCE) calculated from IPCE and UV-Vis spectra shows the same trend between

samples as that of IPCE, which indicates that the enhanced photocathodic current should be ascribed to the improved charge carrier separation and transport. The stability of these films was tested with applied potential at 0.2 V *vs.* RHE. There was no obvious decline in the photocurrent during the range of 300 s. However, in the longer timescale, almost 45% decline in the photocurrent density of BFO_20 was observed in one hour of operation (Fig. S8†), which indicates that the long-term stability of $BiFeO_3$ films needs further optimization.

Light-irradiated Kelvin probe force microscopy (KPFM) was performed to investigate the surface photovoltage (SPV). Contact potential difference (CPD) was recorded in both dark and light illumination condition for each sample. The difference between CPD under dark and light conditions is known as SPV[49] which is shown in Fig. S9.† It was found that BFO_20 possesses the highest SPV at 192 mV. As the magnitude of SPV reflects the ability of minority charge carriers to reach a material's surface,[50] the larger SPV suggests a higher efficiency of photo-generated charge separation.[51] In addition, SPV of $Bi_{1+x}FeO_3$ films generally follows the same trend as their photocathodic current and onset potential (as shown in Fig. S10†), which indicates that the enhanced PEC performance mainly results from the better charge separation efficiency. These results verify that controllable bismuth excess is able to favour separation of photo-generated charges and thus enhance its PEC performance.

Mott–Schottky measurements were performed in order to investigate the interfacial capacitance and charge carrier properties of the samples using a typical Randles equivalent circuit (Fig. S11†). A large frequency dependence of the intercept values was observed, which has been reported previously and ascribed to inhomogeneous current flow in the samples.[52] In addition, it has also been found previously that the presence of surface states and leakage currents due to Fe^{2+} and Fe^{3+} conduction pathways would result in frequency-dependent Mott–Schottky plots.[53,54] As a consequence, it was not possible to obtain reliable flat band potentials from a fit of these curves. However, all samples do show negative slopes confirming the p-type character of all $BiFeO_3$ in agreement with their photocathodic performance, and there is no clear change in carrier density with Bi content, again supporting the conclusion that enhanced charge separation, rather than higher charge carrier density is the main contributing factor for the higher photocurrent in BFO_20 sample.

As it was not possible to derive accurate flat band potentials from Mott–Schottky measurements, the band positions of all $Bi_{1+x}FeO_3$ films including Fermi level, valence band (VB) and conduction band (CB) were measured by combining UPS, XPS and UV-Vis measurements (Fig. S12a†). It is found that there is a general negative trend in the Fermi level position with more Bi content in the electrochemical energy scale, which is in agreement with the literature.[50] Furthermore, the calculated band positions measured in vacuum were used to estimate the band bending that would be generated at the interface when $Bi_{1+x}FeO_3$ film contacts with the electrolyte to reach Fermi level equilibrium, giving an estimation of the flat band potentials ($E_{FB,vac}$). Thus here, $E_{FB,vac}$, are calculated from the band positions in vacuum as −0.1, 0.08, −0.15, −0.27, −0.28, −0.41, and −0.36 V for BFO_0, BFO_5 BFO_10, BFO_15, BFO_20, BFO_25, and BFO_30, respectively. It should be noted that $E_{FB,vac}$ is not the exact flat band potential that will occur in electrochemical process but the estimated value from the band positions in vacuum. As shown in Fig. 4c, $E_{FB,vac}$, becomes slightly more positive as the films go from Bi deficient (BFO_0) towards stoichiometric (BFO_5) and following this gradually become more negative towards BFO_25, levelling out to BFO_30. In the BFO_5 to BFO_20 region this demonstrates an opposite trend to the onset potential, photocurrent and SPV values measured above, indicating that E_{FB} is not the core driving force for increased SPV and thus improved photocurrent and onset potentials in these samples, but there is a more complex interplay of factors, which we discuss in detail below.

Optimizing PEC performance often requires a holistic approach that considers all these factors and their interactions. Considering all the discussion above, nonstoichiometric Bi has a large effect on various factors including morphology, structure, defects, onset potential and electronic properties, which are summarised in Fig. 4c for better understanding of their correlation. Here, the mean grain size shares the same initial trend with photocurrent density but reaches a peak at different points (grain size peaks in BFO_15 while photocurrent density peak in BFO_20). It can be explained that larger grain size is favourable for charge separation in a PEC system[55] and thus leads to higher SPV, more anodic onset potential and photocurrent, but the PEC performance is also affected by oxygen vacancies. As oxygen vacancies may act as recombination sites to deteriorate the separation of photo-generated charges,[37,56] the decreased O_v also contributes the higher SPV and enhanced photocurrent.[57] As shown in Fig. 4c, O_L/O_V generally increases until BFO_20 after which it almost remains constant. O_L/O_V of BFO_20 is higher than that of BFO_15, explaining the peak shift between grain size and photocurrent trends. Meanwhile, the decreased grain size and existence of secondary phase after BFO_20 accounts for the decreased photocurrent with constant oxygen vacancy content. Looking at the estimated flat band potentials, $E_{FB,vac}$, it can be seen that these in general do not correlate with SPV or photocurrent in the BFO_5 to BFO_20 region as discussed above. This implies that the higher SPV values and therefore photocurrent do not originate from an increased energetic driving force for charge injection at the interface, but instead from the improved charge separation due to the increased grain size and reduced defect content. However, the increasingly negative $E_{FB,vac}$ at the highest Bi-content samples (BFO_25 and BFO_30) may contribute to the decreasing photocurrent, since above BFO_20 we observe a large negative shift in the onset potential and drop in SPV, which would reduce photocurrent measured at 0.2 V *vs.* RHE. A more significant factor affecting the photocurrent of BFO_25 and BFO_30, however, may be the secondary phase content, which increases sharply, represented schematically by the impurity peak ($2\theta = 29°$) to $BiFeO_3$ (012) peak ratio in Fig. 4c. This can also explain the rapid drop in photocurrent and SPV above BFO_20, since Bi_2O_3 is expected to have a detrimental

effect on the photocurrent, especially when segregated at the surface as suggested by XPS.

Having identified the optimum stoichiometry for photocurrent generation, it is important to also consider the ferroelectric properties of the samples, therefore PFM response was obtained for $Bi_{1+x}FeO_3$ thin films. The PFM phase images show the distribution of regions with different contrast representing domains with different orientation. In general, the dark region represents the domains oriented toward the substrate (P_{down}) while the bright regions correspond to those oriented toward the film surface (P_{up}). The ferroelectric property of the films was confirmed by the switching of domain orientation. As shown in Fig. 5a, a DC voltage of −8 V was firstly applied on a 4 × 4 μm^2 square of BFO_20, followed by applying +8 V on a 2 × 2 μm^2 square in the centre. The regions with different contrast in unpoled area represents the random spread of domains with different orientations. As shown in the scale bar, bright colour represents upward polarization while dark colour represents downward polarization. According to the change of colour, it can be easily observed that the domains were switched to downward orientation in the 4 × 4 μm^2 region while they were switched to the upward orientation in the central 2 × 2 μm^2 region. PFM switching phase images of BFO_0 and BFO_20 are presented in Fig. S13.† Both also show good ferroelectric switching properties.

After confirming the ferroelectric behaviour of $Bi_{1+x}FeO_3$ thin films, we performed electrochemical (EC) poling (Fig. 5b) on BFO films to orient the polarization of the entire films either P_{in} (positive poled) or P_{out} (negative poled) and measured *J*–*V* curves after the poling treatment. As a result, negatively poled BFO films exhibited an enhanced PEC performance while positively poled samples produced lower photocurrents compared with unpoled samples. It can be explained in terms of the band bending at the electrode interface.[58] Under the condition of negative poling, the spontaneous polarization can induce an internal electric field which results in downward band bending at the interface between the p-type electrode and electrolyte. Such an internal electric field favours separation of photo-generated charges as electrons and holes diffuses towards opposite direction and the downward band bending drives the electrons in the conduction band from the bulk to the interface, where water reduction takes place. In contrast, upward band bending is generated when positively poled, which suppresses the transportation of electrons to the interface and leads to decreased PEC performance, which is illustrated in Fig. 5c. This is confirmed by the PEC measurement. As shown in Fig. 5d and e, the negatively-poled BFO_20 film shows an enhancement of the photocurrent of about 27.3 μA cm^{-2} (more than 100%) compared to the unpoled film at 0.4 V *vs.* RHE. In contrast, positive poling decreases the photocurrent

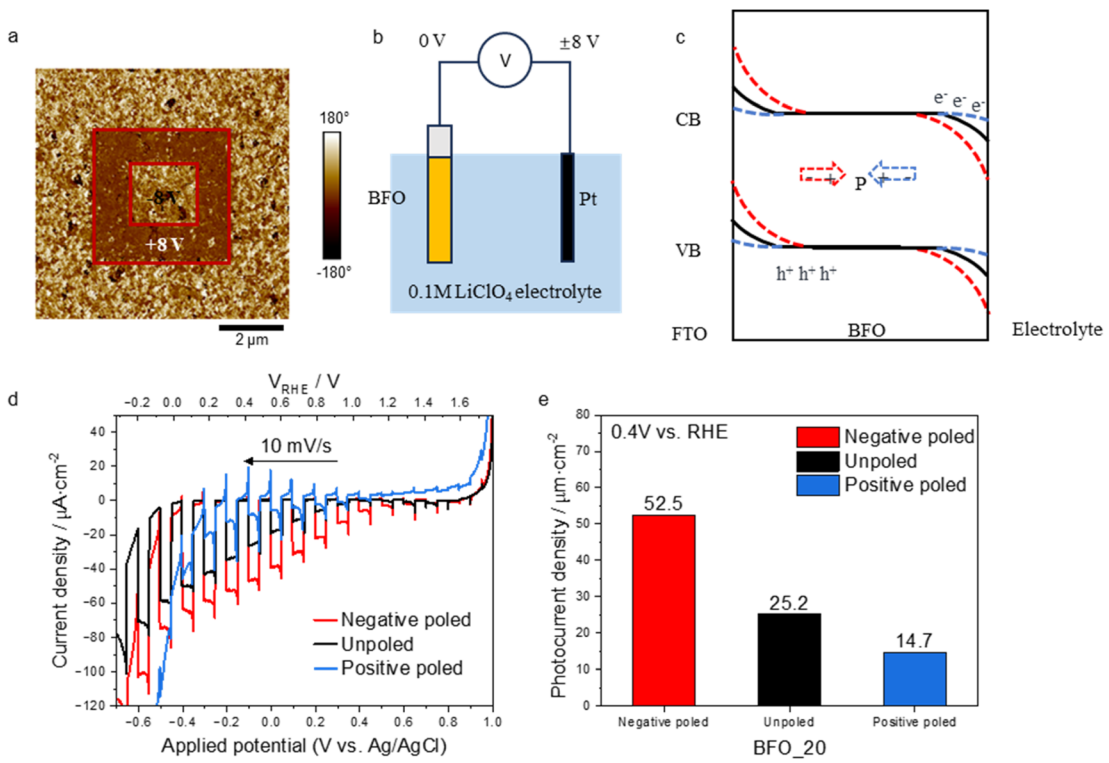

Fig. 5 (a) PFM phase signals of BFO_20 film in an 8 × 8 μm^2 region which is polarized with +8 V in a 4 × 4 μm^2 region firstly and then polarized with −8 V in a 2 × 2 μm^2 region in the centre. (b) Electrochemical poling set up. (c) Schematic of the band structure of BFO films which shows the band bending of unpoled (black), negative-poled (red) and positive-poled (blue) BFO films. (d) LSV measurements of unpoled, negative-poled and positive-poled BFO_20 thin films under chopped illumination in 0.2 M Na_2SO_4 electrolyte. (e) The photocurrent density of unpoled and poled BFO_20 films obtained at 0.4 V *vs.* RHE.

density by around 10.5 μA cm^{-2} compared to the unpoled film at 0.4 V *vs.* RHE.

4. Conclusions

In the present work, we synthesized and studied $Bi_{1+x}FeO_3$ thin films prepared by a simple chemical solution deposition method using different amounts of bismuth in the precursor. It was found that an appropriate excess bismuth in BFO produces an enhancement of photocathodic performance. The best film has 20% excess Bi added (BFO_20, in reality $Bi_{1.14\pm0.02}FeO_3$ based on EDX) showed an enhancement of the photocurrent density around 66.6% compared to the BFO film close to stoichiometry. As the optical properties do not change, the enhanced PEC performance can be ascribed to the improved electronic properties of the samples leading to improved charge separation, which was confirmed by SPV measurements. Further analysis showed that the enhanced photocurrent and electronic properties are attribute to multiple factors including structure, morphology and defects. The grain size was found to increase firstly, reaching the maximum mean size of 0.27 μm in BFO_15 and then decrease due to the formation of Bi_2O_3. The larger grains are beneficial to the transportation of photo-generated charges. Oxygen vacancies generally decrease with increasing amounts of bismuth which also favours the separation of photo-generated charges. Additionally, such variations in morphology and defects are accompanied by a change in structure. Moreover, the ferroelectric properties were confirmed by PFM. The switch of spontaneous polarization was clearly observed in BFO films. There was a significant improvement in photocurrent after performing −8 V electrochemical poling on BFO_20. It suggests that ferroelectric poling with correct orientation is very favourable when BFO with excess bismuth is used as photocathode.

Above all, this research indicates that $BiFeO_3$ with deficient bismuth should be avoided carefully due to the volatility of bismuth during heat treatment. And the enhanced PEC response of self-doped $Bi_{1+x}FeO_3$ thin films has been demonstrated, which gives a simple modification method without extrinsic dopants. However, it is important to stress that benefit arise from a very complex set of changes in the samples, including structure, morphology, defects and electronic properties, highlighting the need to analyse all of these properties together to understand the underlying factors behind increased photocurrent in any photoelectrodes. Moreover, negative electrochemical poling can further improve the photocathodic water splitting performance. As this work studies $BiFeO_3$ itself without any other element or alteration, it could be of benefit to all studies on $BiFeO_3$-based ferroelectric materials for PEC application.

Data availability

Data for this article, including raw measurement data and original, full resolution micrograph images are available at Queen Mary Research Online (QMRO) at **https://qmro.qmul.ac.uk/xmlui/**.

Author contributions

Haozhen Yuan and Joe Briscoe planned and designed the experimental methodology. Haozhen Yuan led and performed all experiments other than PFM characterization, which he performed with Subhajit Pal, and SEM measurements, which he performed with Qinrong He. Chloe Forrester performed measurement and calculations for IPCE and APCE spectra. Haozhen Yuan drafted the manuscript, which was edited by Joe Briscoe and Subhajit Pal.

Conflicts of interest

There are no conflicts to declare.

Acknowledgements

This project received funding from the China Scholarship Council (CSC) and the European Research Council (ERC) under the European Union's Horizon 2020 research and innovation programme (grant agreement no. 101001626). The authors thank Dr Richard Whiteley for carrying out XRD measurements and Prof. Ana Jorge Sobrido for the LED light source for KPFM measurements.

References

1 N. R. Yogamalar, S. Kalpana, V. Senthil and A. Chithambararaj, *Multifunct. Photocatal. Mater. Energy*, 2018, 307–324.
2 G. Liu, S. K. Karuturi, H. Chen, D. Wang, J. W. Ager, A. N. Simonov and A. Tricoli, *Sol. Energy*, 2020, **202**, 198–203.
3 Y. Li, J. Li, W. Yang and X. Wang, *Nanoscale Horiz.*, 2020, **5**, 1174–1187.
4 Y. Yu and X. Wang, *Adv. Mater.*, 2018, **30**, 1800154.
5 G. Liu, L. Ma, L. C. Yin, G. Wan, H. Zhu, C. Zhen, Y. Yang, Y. Liang, J. Tan and H. M. Cheng, *Joule*, 2018, **2**, 1095–1107.
6 G. Wan, L. Yin, X. Chen, X. Xu, J. Huang, C. Zhen, H. Zhu, B. Huang, W. Hu, Z. Ren, H. Tian, L. Wang, G. Liu and H. M. Cheng, *J. Am. Chem. Soc.*, 2022, **144**, 20342–20350.
7 S. V. Kalinin, D. A. Bonnell, T. Alvarez, X. Lei, Z. Hu, J. H. Ferris, Q. Zhang and S. Dunn, *Nano Lett.*, 2002, **2**, 589–593.
8 A. Augurio, A. Alvarez-Fernandez, V. Panchal, B. Pittenger, P. De Wolf, S. Guldin and J. Briscoe, *ACS Appl. Mater. Interfaces*, 2022, **14**, 13147–13157.
9 P. Senthilkumar, D. A. Jency, T. Kavinkumar, D. Dhayanithi, S. Dhanuskodi, M. Umadevi, S. Manivannan, N. V. Giridharan, V. Thiagarajan, M. Sriramkumar and K. Jothivenkatachalam, *ACS Sustain. Chem. Eng.*, 2019, **7**, 12032–12043.
10 S. Samanta, V. Sankaranarayanan and K. Sethupathi, *Vacuum*, 2018, **156**, 456–462.
11 D. Lebeugle, D. Colson, A. Forget and M. Viret, *Appl. Phys. Lett.*, 2007, **91**, 022907.
12 J. X. Zhang, Q. He, M. Trassin, W. Luo, D. Yi, M. D. Rossell, P. Yu, L. You, C. H. Wang, C. Y. Kuo, J. T. Heron, Z. Hu,

R. J. Zeches, H. J. Lin, A. Tanaka, C. T. Chen, L. H. Tjeng, Y. H. Chu and R. Ramesh, *Phys. Rev. Lett.*, 2007, **107**, 147602.
13 J. Wang, J. B. Neaton, H. Zheng, V. Nagarajan, S. B. Ogale, B. Liu, D. Viehland, V. Vaithyanathan, D. G. Schlom, U. V. Waghmare, N. A. Spaldin, K. M. Rabe, M. Wuttig and R. Ramesh, *Science*, 2003, **299**, 1719–1722.
14 C. Ederer and N. A. Spaldin, *Phys. Rev. Lett.*, 2005, **95**, 257601.
15 J. Li, J. Wang, M. Wuttig, R. Ramesh, N. Wang, B. Ruette, A. P. Pyatakov, A. K. Zvezdin and D. Viehland, *Appl. Phys. Lett.*, 2004, **84**, 5261–5263.
16 H. Ba, M. Bibes, X. H. Zhu, S. Fusil, K. Bouzehouane, S. Petit, J. Kreisel and A. Barthĺmy, *Appl. Phys. Lett.*, 2008, **93**, 072901.
17 D. Sando, A. Barthélémy and M. Bibes, *J. Phys.: Condens.Matter*, 2014, **26**, 473201.
18 Q. Liu, Y. Zhou, L. You, J. Wang, M. Shen and L. Fang, *Appl. Phys. Lett.*, 2016, **108**, 022902.
19 Y. Wang, M. Zhang, Y. Yue, H. Zhang, A. Mahajan, S. Dunn and H. Yan, *Sol. RRL*, 2022, **6**, 2200124.
20 P. Sharma, P. K. Diwan and O. P. Pandey, *Mater. Chem. Phys.*, 2019, **233**, 171–179.
21 G. Y. Zhang, J. Q. Dai and Y. S. Lu, *J. Mater. Sci.: Mater. Electron.*, 2021, **32**, 10289–10298.
22 X. Xie, S. Yang, F. Zhang, S. Fan, Q. Che, C. Wang, X. Guo and L. Zhang, *J. Mater. Sci.: Mater. Electron.*, 2015, **26**, 10095–10101.
23 S. Tian, C. Wang, Y. Zhou, X. Li, P. Gao, J. Wang, Y. Feng, X. Yao, C. Ge, M. He, X. Bai, G. Yang and K. Jin, *ACS Appl. Mater. Interfaces*, 2018, **10**, 43792–43801.
24 A. Kumari, K. Kumari, F. Ahmed, M. M. Ahmad, J. Sharma, A. Vij and S. Kumar, *J. Mater. Sci.: Mater. Electron.*, 2021, **32**, 23968–23982.
25 S. Gupta, M. Tomar, V. Gupta, A. R. James, M. Pal, R. Guo and A. Bhalla, *J. Appl. Phys.*, 2014, **115**, 234105.
26 B. P. Reddy, M. C. Sekhar, B. P. Prakash, Y. Suh and S. H. Park, *Ceram. Int.*, 2018, **44**, 19512–19521.
27 X. Yin, C. Chen, Z. Fan, M. Qin, M. Zeng, X. Lu, G. Zhou, X. Gao, D. Chen and J. M. Liu, *Mater. Today Phys.*, 2021, **17**, 100345.
28 P. Kumar, C. Panda and M. Kar, *Smart Mater. Struct.*, 2015, **24**, 045028.
29 M. M. Rhaman, M. A. Matin, M. N. Hossain, F. A. Mozahid, M. A. Hakim, M. H. Rizvi and M. F. Islam, *J. Electron. Mater.*, 2018, **47**, 6954–6958.
30 S. K. Pradhan, J. Das, P. P. Rout, S. K. Das, D. K. Mishra, D. R. Sahu, A. K. Pradhan, V. V. Srinivasu, B. B. Nayak, S. Verma and B. K. Roul, *J. Magn. Magn. Mater.*, 2010, **322**, 3614–3622.
31 N. Zhang, D. Chen, F. Niu, S. Wang, L. Qin and Y. Huang, *Sci. Rep.*, 2016, **6**, 26467.
32 D. Wang, M. Wang, F. Liu, Y. Cui, Q. Zhao, H. Sun, H. Jin and M. Cao, *Ceram. Int.*, 2015, **41**, 8768–8772.
33 Y. Han, W. Mao, C. Quan, X. Wang, J. Yang, T. Yang, X. Li and W. Huang, *Mater. Sci. Eng., B*, 2014, **188**, 26–30.
34 A. S. Priya, D. Geetha and Ş. Ţălu, *Mater. Lett.*, 2020, **281**, 128615.
35 J. Z. Huang, Y. Shen, M. Li and C. W. Nan, *J. Appl. Phys.*, 2011, **110**, 094106.
36 L. Bai, M. Sun, W. Ma, J. Yang, J. Zhang and Y. Liu, *Nanomaterials*, 2020, **10**, 1–13.
37 Z. Wang and L. Wang, *EcoMat*, 2021, **3**, e12075.
38 S. J. Jeong, K. H. Kim and H. J. Ahn, *Ceram. Int.*, 2022, **48**, 9400–9406.
39 S. Chu, W. Li, Y. Yan, T. Hamann, I. Shih, D. Wang and Z. Mi, *Nano Futures*, 2017, **1**, 22001.
40 M. Rioult, S. Datta, D. Stanescu, S. Stanescu, R. Belkhou, F. Maccherozzi, H. Magnan and A. Barbier, *Appl. Phys. Lett.*, 2015, **107**, 103901.
41 Y. Wang, J. Zhang, M. S. Balogun, Y. Tong and Y. Huang, *Mater. Today Sustain.*, 2022, **18**, 100118.
42 Y. Huang, B. Long, M. Tang, Z. Rui, M. S. Balogun, Y. Tong and H. Ji, *Appl. Catal., B*, 2016, **181**, 779–787.
43 C. Quan, Y. Han, N. Gao, W. Mao, J. Zhang, J. Yang, X. Li and W. Huang, *Ceram. Int.*, 2016, **42**, 537–544.
44 F. Yan, T. J. Zhu, M. O. Lai and L. Lu, *Scr. Mater.*, 2010, **63**, 780–783.
45 P. S. V. Mocherla, C. Karthik, R. Ubic, M. S. Ramachandra Rao and C. Sudakar, *Appl. Phys. Lett.*, 2013, **103**, 022910.
46 S. Yang, G. Ma, L. Xu, C. Deng and X. Wang, *RSC Adv.*, 2019, **9**, 29238–29245.
47 P. MacHado, I. Canõ, C. Menéndez, C. Cazorla, H. Tan, I. Fina, M. Campoy-Quiles, C. Escudero, M. Tallarida and M. Coll, *J. Mater. Chem. C*, 2021, **9**, 330–339.
48 S. Das, P. Fourmont, D. Benetti, S. G. Cloutier, R. Nechache, Z. M. Wang and F. Rosei, *J. Chem. Phys.*, 2020, **153**, 084705.
49 V. Donchev, *Mater. Res. Express*, 2019, **6**, 103001.
50 B. Tan, A. M. Reyes, E. Menéndez-Proupin, S. E. Reyes-Lillo, Y. Li and Z. Zhang, *ACS Energy Lett.*, 2022, **7**, 3492–3499.
51 D. Cavalcoli, B. Fraboni and A. Cavallini, in *Semiconductors and Semimetals*, Academic Press Inc., 2015, vol. 91, pp. 251–278.
52 S. P. Harrington and T. M. Devine, *J. Electrochem. Soc.*, 2008, **155**, C381.
53 A. Hankin, F. E. Bedoya-Lora, J. C. Alexander, A. Regoutz and G. H. Kelsall, *J. Mater. Chem. A*, 2019, **7**, 26162–26176.
54 K. H. Saeed, D. A. Garcia Osorio, C. Li, L. Banerji, A. M. Gardner and A. J. Cowan, *Chem. Sci.*, 2023, **14**, 3182–3189.
55 H. L. Tan, R. Amal and Y. H. Ng, *ACS Appl. Mater. Interfaces*, 2016, **8**, 28607–28614.
56 Y. Huang, Y. Yu, Y. Yu and B. Zhang, *Sol. RRL*, 2020, **4**, 2000037.
57 Z. Wang, X. Mao, P. Chen, M. Xiao, S. A. Monny, S. Wang, M. Konarova, A. Du and L. Wang, *Angew. Chem.*, 2019, **131**, 1042–1046.
58 S. Casadio, A. Gondolini, N. Sangiorgi, A. Candini and A. Sanson, *Sustainable Energy Fuels*, 2022, **7**, 1107–1118.